Earth Planet. Sci. Lett. 634 (2024) 118674

Contents lists available at ScienceDirect

Earth and Planetary Science Letters

journal homepage: www.elsevier.com/locate/epsl

The pace of global river meandering influenced by fluvial sediment supply

Evan Greenberg [a,*], Vamsi Ganti [a,b]

[a] Department of Geography, University of California Santa Barbara, Santa Barbara, CA 93106, United States
[b] Department of Earth Science, University of California Santa Barbara, Santa Barbara, CA 93106, United States

ARTICLE INFO

Editor: J.P. Avouac

Keywords:
Geomorphology
Sediment flux
River mobility
Remote sensing
Meandering
Vegetation

ABSTRACT

Meandering rivers move gradually across the floodplains, and this river movement presents socioeconomic risks along river corridors and regulates terrestrial biogeochemical cycles. Experimental and field studies suggest that fluvial sediment supply can exert a primary control on lateral migration rates of rivers. However, we lack an understanding of the relative importance of environmental boundary conditions, such as floodplain vegetation and sediment supply, in setting the pace of river meandering across different environmental settings. Here, we combine the analysis of satellite imagery and global-in-scale sediment and water discharge models to evaluate the controls on lateral migration rates of 139 meandering rivers that span a wide range in size, climate, and bank vegetation. We show that migration rates normalized by the channel width monotonically increase with the volumetric sediment flux normalized by the characteristic size of the river. This relation is consistent across rivers in vegetated and unvegetated catchments, indicating that enhanced lateral migration rates in unvegetated basins is likely not only facilitated by lower bank mechanical strength, but also by higher normalized sediment supply in ephemeral rivers. Using three case examples, we also demonstrate that width-normalized meander migration rates respond to spatial gradients in sediment supply caused by river impoundments, highlighting the prominent role of sediment supply in setting the pace of meander migration. Our results suggest that sediment-supply variations caused by climate, land-cover and land-use changes can lead to predictable changes in meandering river evolution and ultimately drive architectural changes in sedimentary stratigraphy.

1. Introduction

Meandering rivers are ubiquitous in Earth's lowland regions. Meandering river corridors can be densely populated regions (Zhu et al., 2007), which serve as centers of agriculture (Micheli et al., 2004), and their depositional products are often used to interpret past hydrological conditions on Earth and Mars (Barefoot et al., 2021; Cardenas et al., 2017; Foreman et al., 2012). The geomorphic processes active within meandering river systems impact the terrestrial residence time of organic carbon (Repasch et al., 2021; Torres et al., 2017), basin-wide biochemical fluxes (Gomez-Velez et al., 2015), and can be factors in the management of erosion hazards within floodplains (Best, 2019; Ollero, 2010). Projected extreme environmental changes can impact the geomorphic evolution of meandering rivers over human timescales (Papalexiou and Montanari, 2019). However, our ability to forecast the response of meandering rivers to shifts in environmental boundary conditions, such as sediment and water discharge as well as land-use and land-cover changes, remains incomplete.

Lateral migration is the dominant geomorphic process in meandering rivers over decadal timescales. Lateral migration rates vary within a given reach and across different reaches. Channel planform curvature, which introduces asymmetry to the fluid flow through the river bend (Struiksma et al., 1985), is considered to be the primary control on varying lateral migration rates at the bend scale (Furbish, 1988; Sylvester et al., 2019). The impact of channel curvature may be non-local, whereby the strength of the curvature-driven excess bank-directed shear stress is impacted by the upstream curvatures for a given bend (Ikeda et al., 1981). River reaches worldwide also show order-of-magnitude differences in lateral migration rates when averaging across reach scales (i.e., scale of multiple bends) (e.g., Hickin and Nanson, 1984). Environmental factors like gradients of fluvial sediment supply and differences in riverbank vegetation may impact lateral migration rates, explaining some reach-to-reach variability in lateral migration rates (Church, 2006; Constantine et al., 2014; Donovan et al., 2021; Ielpi et al., 2022; Ielpi and Lapôtre, 2020; Micheli and Kirchner, 2002).

Bank vegetation increases the propensity for stable river meandering

* Corresponding author.
E-mail address: egreenberg@ucsb.edu (E. Greenberg).

https://doi.org/10.1016/j.epsl.2024.118674
Received 5 October 2023; Received in revised form 6 March 2024; Accepted 11 March 2024
Available online 23 March 2024

by enhancing bank mechanical strength (Braudrick et al., 2009; Tal and Paola, 2007). An analysis of 40 rivers across varying climate shows that river bends with unvegetated banks have an order-of-magnitude faster migration rates than bends with vegetated banks when normalized by their width (Ielpi and Lapôtre, 2020). Alternatively, increases in sediment supply are linked to reach-scale variations in lateral migration rates of meandering rivers (Constantine et al., 2014). Sediment supply is linked to the deposition of point-bar sediment on the inner bend of channels, which alters fluid flow asymmetry and further drives outer-bank erosion (Dietrich and Smith, 1983). Previous empirical studies have sought to support the linkage between sediment supply and lateral migration rate. A notable example is within the Amazon basin, where large meandering rivers with high suspended sediment loads are correlated with fast lateral migration rates (Ahmed et al., 2019; Constantine et al., 2014). In contrast, a recent remote sensing study found no correlation between lateral migration rates and modeled sediment supply for large rivers with widths greater than 150 m (Langhorst and Pavelsky, 2023). Furthermore, experimental studies also focused on how environmental factors impact river mobility, and found a power-law dependence between lateral migration rates and the magnitude of sediment supply relative to the size of the channel across single-thread and multi-thread rivers (Bufe et al., 2019; Wickert et al., 2013).

Despite these advances, we currently lack studies that integrate sediment supply, floodplain vegetation, and lateral migration rates within the same framework and across a dataset that is representative of the full range of variability present in meandering river basins worldwide. The availability of high-resolution satellite imagery over the last three decades and proliferation of published reach-scale lateral migration rates now provides an ideal opportunity to assess primary environmental controls on lateral migration rates in meandering rivers. We leverage satellite observations of meandering river planform changes to assess reach-scale lateral migration rates for 139 rivers with vegetated, sparsely vegetated and unvegetated channel banks (Fig. 1). Using a framework based on experimental hypotheses, we demonstrate that the pace of lateral migration is proportional to the volumetric sediment supply relative to the characteristic point-bar volume. We also pair the cross-river comparison with case studies of three dammed North American rivers to examine the impact of extreme gradients in sediment supply on downstream changes in river mobility within individual rivers. Finally, we discuss the implications of our findings in the context of river response to future climate and land-use changes, and in interpreting singular changes in the architecture of fluvial strata.

2. Theoretical framework

A characteristic property of meandering rivers is that their channel widths are approximately constant over decadal timescales (Mason and Mohrig, 2019). A mass balance framework is a reasonable assumption for meandering river migration at a decadal timescale, which assumes that the rate at which material is removed along a cut bank is balanced by the deposition of material on the point bar (Church, 2006). This balance can be written as:

$$M_r \approx v_{d,y} \tag{1}$$

where M_r is the migration rate of the cut bank in m/yr and $v_{d,y}$ is the transverse sediment deposition rate in m/yr (Fig. 2). While the

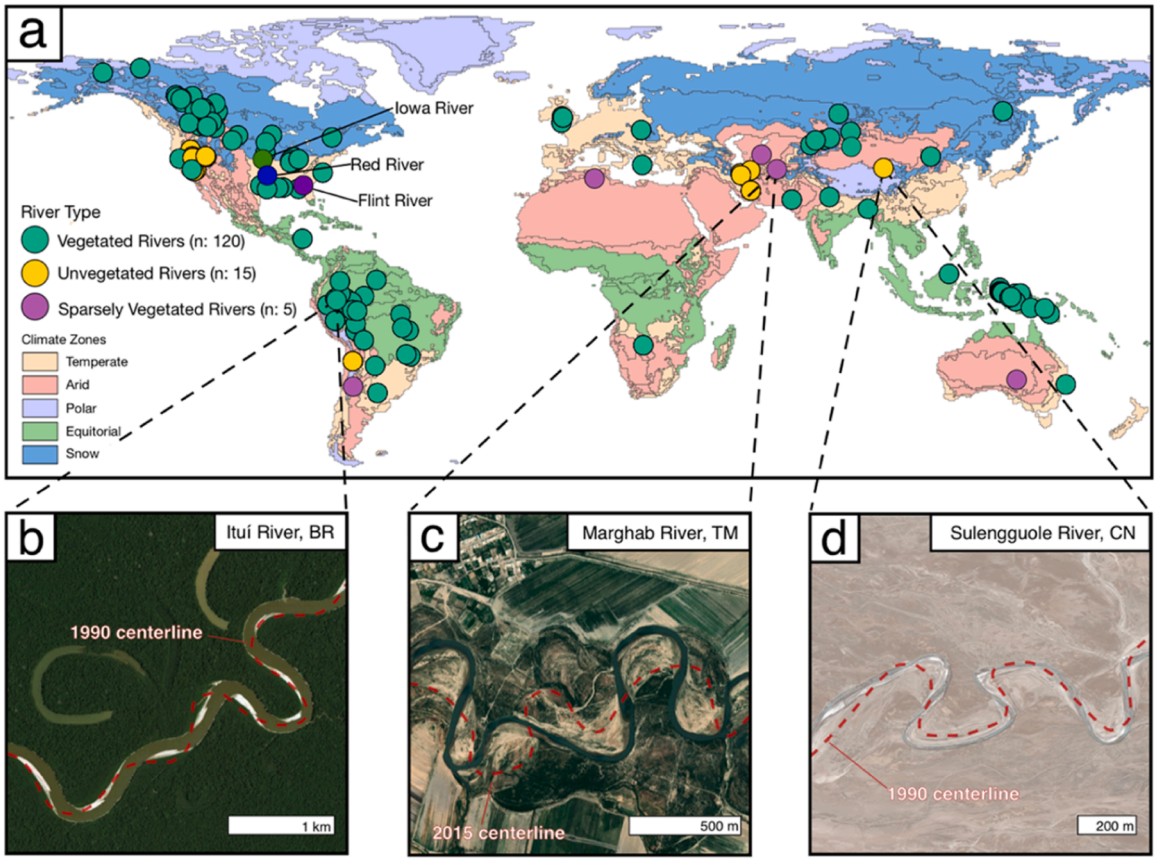

Fig. 1. Study locations and example rivers. (a) Locations of the 139 rivers included in this study. River floodplain types are shown in teal (vegetated), orange (unvegetated), and light purple (sparse). Location of the three impoundment case studies are labeled. The basemap shows the five main Köppen climate groups (Peel et al., 2007). Examples of meandering rivers with (b) vegetated floodplains, (c) sparsely-vegetated floodplains and (d) unvegetated floodplains. The dotted red lines are previous channel centerline positions. All images (Copyright Maxar Technologies) are obtained through Google Earth Pro for the years 2020, 2019, and 2013, respectively.

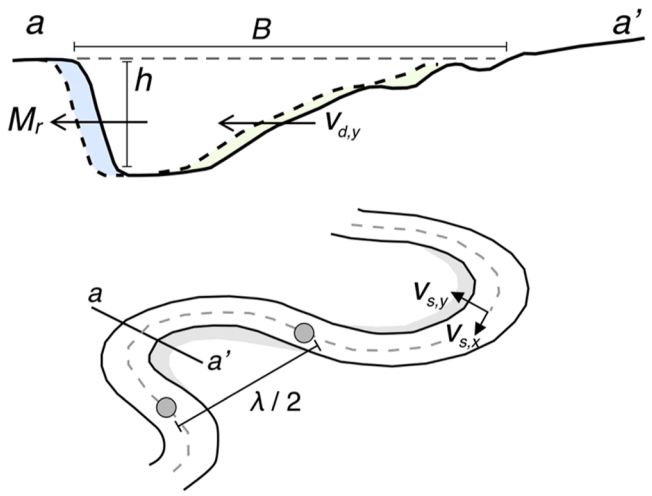

Fig. 2. Schematic highlighting the variables in the theoretical framework. A cross-section view of a point bar apex (top), and a plan-view of a meandering river (bottom). Variables are noted where B is the bankfull channel width, h is the bankfull channel depth, $v_{d,y}$ is the transverse sediment deposition rate, $v_{s,x}$ is the cross-section average downstream sediment transport rate, $v_{s,y}$ is the transverse sediment transport rate, $\lambda/2$ is the distance between adjacent inflection points equal to one half the meander wavelength, and M_r is the retreat rate of the cut bank.

theoretical mass balance hinges on the lateral sediment deposition rate, most readily available sediment data reports downstream sediment flux. To connect the two, we first assume that the lateral sediment deposition rate is proportional to the transverse sediment transport rate, $v_{s,y}$: $v_{d,y} \propto v_{s,y}$. Further, the transverse bed-material sediment transport rate is a function of the downstream bed-material sediment transport rate, transverse bed slope, and grain size (Sekine and Parker, 1992). We then assume that the transverse sediment transport rate is proportional to the cross-section average downstream sediment transport rate, $v_{s,x}$ in m/yr. We recast $v_{s,x}$ in terms of the volumetric sediment flux, Q_s, as:

$$v_{s,x} = \frac{Q_s}{hB} \tag{2}$$

where h and B are bankfull channel depth and width, respectively (Fig. 2). Finally, following Wickert et al. (2013), we substitute Eq. (2) in (1) and normalize the migration rate by channel width to control for the effect of river size (following Constantine et al., 2014; Donovan et al., 2021; Hickin and Nanson, 1984), which yields:

$$\frac{M_r}{B} \propto \frac{Q_s}{hB^2} \tag{3}$$

We note that the downstream sediment flux is an imperfect proxy for sediment deposition rate, which more accurately represents the local gradient in sediment flux (Church, 2006). However, downstream bed-material flux provides an upper limit on the depositional rate and should represent the magnitude of sediment flux available for deposition.

Eq. (3) describes that the width-normalized lateral migration rate is proportional to the magnitude of sediment flux available for deposition relative to a characteristic volume of the mobile sedimentary deposit—the point bar. Bar size is set by channel-thread geometry (Greenberg et al., 2021; Holzweber et al., 2014; Mohrig et al., 2000), which in turn is set by the formative water discharge (Leopold and Maddock, 1953). This suggests that sediment flux relative to water discharge (i.e., sediment concentration) should be similarly related to the lateral migration rate, which is a hypothesis emerging from generalized studies of experimental rivers (Bufe et al., 2019; Wickert et al., 2013). We note that Eq. (3) is the inverse of lateral migration and sediment supply timescales of Torres et al. (2017).

Channel depths are difficult to estimate from multispectral remote data without site-specific model training (Legleiter et al., 2009). We instead use the meander wavelength, λ, as an alternate length scale relevant to the point bar. Meander wavelengths are important for sediment travel distances in meandering rivers and potentially the mass balance in lateral migration (Church, 2006; Neill, 1971). Replacing depth with wavelength in Eq. (3) yields:

$$M_r^* \propto Q_s^* \tag{4}$$

where M_r^* is the normalized migration rate in 1/yr:

$$M_r^* = \frac{M_r}{B} \tag{5a}$$

and Q_s^* is the normalized fluvial sediment supply in 1/yr:

$$Q_s^* = \frac{Q_s}{\lambda B^2} \tag{5b}$$

We evaluated Eq. (4) for meandering rivers across a wide range of environmental settings as well as individual rivers that have downstream sediment supply gradients created by dam impoundments.

3. Materials and methods

3.1. Sampling meandering rivers

We built a database of 139 meandering river reaches spanning 6 continents and all climate zones (Fig. 1(a)). We directly measured reach-scale migration rates for 55 river reaches using multispectral time series from Landsat images (Fig. 1), accessible through Google Earth Engine (Gorelick et al., 2017). We complemented these measurements by integrating 84 published reach-scale migration rates (Table S1). Our approach aimed to aggregate existing migration rate compilations while expanding the dataset's geographic and scale representation. The published databases predominantly focused on rivers in North and South America. Further, the channel widths of meandering rivers in unvegetated basins with published migration rates are significantly smaller than Landsat resolution (30 m). Our primary sampling strategy addressed these gaps by incorporating meandering rivers in Central Asia and Papua New Guinea, regions with many meandering rivers but largely absent from published compilations. Additionally, we attempted to include unvegetated and sparsely vegetated meandering reaches with widths more comparable to the vegetated meandering reaches. We were only able to contribute one new migration rate measurement for an unvegetated reach (Sulengguole River) that has comparable width (~60 m) to the vegetated meandering rivers in the database. The final database encompasses 119 vegetated, 5 sparsely vegetated and 15 unvegetated meandering rivers, spanning from 33.10° S to 67.67° N in latitude, with measured widths ranging from 3.2 m to 4400 m. Bank vegetation classifications are based on the percentage of area covered by vegetation in the surrounding floodplain (Supplementary Text S1).

3.2. Estimation of lateral migration rates of meandering rivers

We used a multi-step process to measure lateral migration rates. Our procedure 1) generated binary channel masks from remote imagery, 2) generated channel centerlines from binary channel masks, and 3) used a dynamic time warping (DTW) algorithm to estimate migration distances from successive channel centerlines. We generated water masks from annual median composite images from Landsat 5 TM, Landsat 7 ETM+ and Landsat 8 OLI/TIRS surface reflectance data sets available through Google Earth Engine. Annual compositing removes some of the intra-annual variability in river stage in the resulting images (Schwenk et al., 2017). Each annual composite image included spectral information for bands ranging from blue to SWIR wavelengths (Fig. 3(a)). We downloaded the 7-band annual composite images from a reach scale

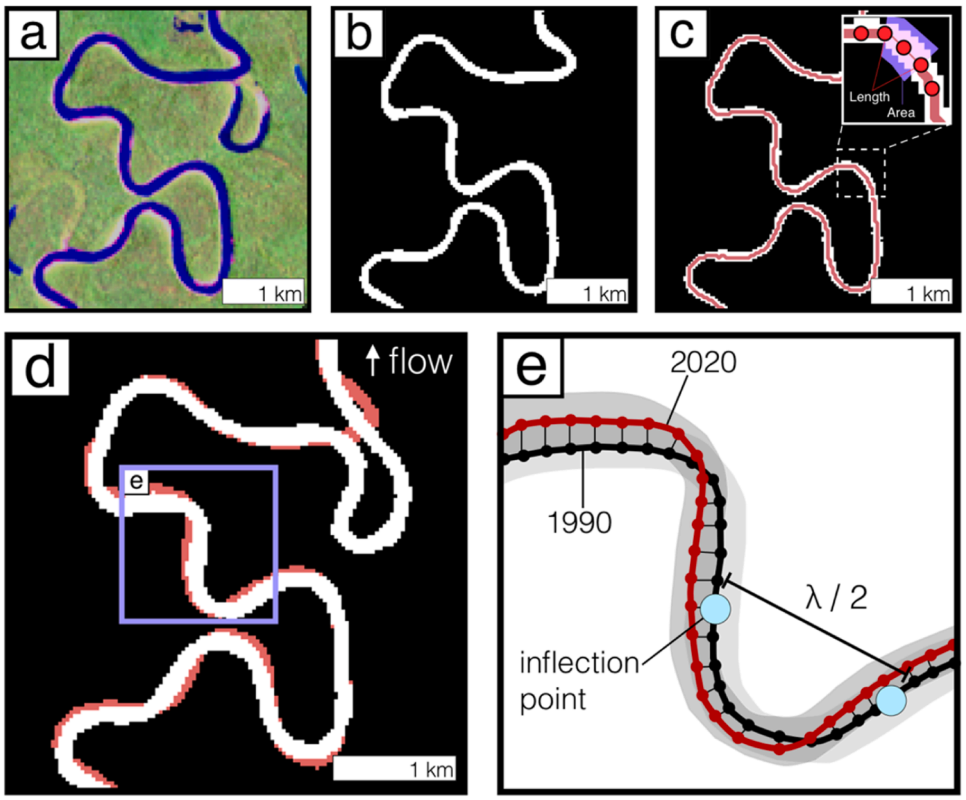

Fig. 3. Remote sensing methods to measure channel widths and migration distances. (a) Landsat (Shortwave Infrared, Near Infrared, Green) composite of the Ituí River, BR. (b) Generated channel mask using the DSWE partial surface water classification threshold (Jones, 2019). (c) River channel mask with derived channel centerline (red). Inset shows the scheme to estimate channel widths using the intersection between the purple region and the white channel mask. (d) Overlapping channel masks from 1990 to 2020. Migrated area is shown in light red. (e) Channel centerline point matching using Dynamic Time Warping algorithm (Sylvester et al., 2019).

over 15–25 channel bends. We produced binary water masks from annual composite multispectral data by utilizing the USGS Dynamic Surface Water Extent (DSWE) method (Jones, 2019). The DSWE algorithm uses an expert-tuned decision-tree structure between several spectral indices, which provides water classification and an estimate of classification confidence (high, medium, partial, and aggressive-partial). For our water masks, we used the partial-surface water classification, which includes high, medium, and partial classified surface water. The DSWE algorithm generates binary water masks encompassing all types of inland waters, not just river channels. We used an established method to reduce surface water masks to channel masks (Yang et al., 2019). This procedure collocated vector products of predicted channel location (Allen and Pavelsky, 2018) with the classified surface water area, and used a 1 km buffer to filter out any classified water that is not connected to the river (Fig. 3(b)).

We generated channel centerlines by a skeletonization of the channel masks, followed by recursive pruning to remove unwanted spurs, manual cleaning, and a nearest-neighbor smoothing. We measured channel widths from the channel centerlines and binary channel masks. We sampled points along the centerline at even one-pixel spacings. Centered on each centerline point, we drew a polygon of downstream length equal to the distance between the upstream and downstream point and cross-stream width greater than a manually estimated channel width. The channel width, B, was then calculated as the intersection between polygon area and the channel mask divided by the downstream length of the polygon (Fig. 3(c)). The width was measured for each sampled centerline point.

There is a range of techniques to estimate lateral migration rates (Fig. 3(d)) from remote data (Chadwick et al., 2023; Hickin and Nanson, 1984; Ielpi and Lapôtre, 2020; Langhorst and Pavelsky, 2023; Rowland et al., 2016; Schwenk et al., 2017). The lateral migration of the channel centerline is a reasonable approximation of paired bank-bar migration, and comparing two successive channel centerlines provides an estimate of channel displacement. We used a DTW algorithm to match equivalent points from one centerline to another (Fig. 3(e)). This algorithm eliminates ambiguity in matching equivalent centerline points (Sylvester et al., 2019). We recorded migration distances at the same spacing as channel widths, and manually filtered out any migration pairs that fell within channel-bend cutoffs. We aggregated these measurements at the bend scale by computing the median of migration distances between successive centerline inflection points (Fig. 3(e)). We also aggregated measurements at the reach scale by computing the mean of the bend-scale measurements within the entire observation window. We used the time between successive channel centerlines to calculate lateral migration rates, and this duration varied within our dataset. For fast migrating rivers, we used the time necessary to migrate roughly one channel width. For slow migrating rivers, we used a 30-year observation period (1990–2020) (Fig. 3(d)). The measured migration distances are not dependent on observation period (Figs. S1–2).

To supplement our primary-collected migration rates, we collated 84 additional reach-scale migration rates from published databases and literature (Table S1). Collating data from literature sources allowed us to include rivers below the threshold of Landsat resolution. The DSWE workflow described above could measure rivers of width greater than 40 m, and the narrowest in that range could only be achieved with manual intervention to create water masks and channel centerlines. The "centerlines" in the case of narrowest primary collected rivers represent the channel masks themselves. With published sources, we included rivers with width up to 3 m (Ielpi and Lapôtre, 2020). We curated the data to only include rivers with evidence of active channel-belt evolution (i.e.,

abandoned meanders and scroll bar formation). We disqualified rivers with evidence of entrenchment, and those found in distributary settings as the water and sediment discharge are distributed into multiple active threads. The published sources use different techniques to derive lateral migration rates (DTW, bend-apex tracking, area-based approaches). In an overlapping set of rivers, we found that lateral migration rates derived across these common methods were consistent (Fig. S3).

3.3. Quantifying sediment supply and stream power

We used water and sediment discharge data, spanning 1980 to 2020, from the WBMsed model (Cohen et al., 2013, 2022). The model uses the HydroSHEDS (Lehner et al., 2008) drainage basin product to produce drainage network masks, pairs a high temporal-resolution water discharge model (Wisser et al., 2010) with the empirical BQART sediment yield model to generate suspended sediment flux estimates. The model also has a modified version of Lammers and Bledsoe (2018) relation to generate bedload sediment flux estimates as well as the portion of the suspended load that interacts with the bed (Cohen et al., 2022). The detailed implementation and validation of the model is found in the originating articles (Cohen et al., 2013, 2014, 2022). While the sediment fluxes used here are modeled values, they provide reasonable order-of-magnitude estimates of expected sediment fluxes based on the basin area, topography, climate, and modeled daily discharge. Field measurements of bedload sediment flux are difficult to obtain over representative timescales and are therefore scarce for the vast majority of rivers (Turowski et al., 2010). The WBMsed model provides a scalable methodology to track sediment fluxes across a wide range of rivers in geographically disparate regions. It is important to note, however, that uncertainty in model results are especially pertinent in the arid catchments represented in our dataset, which are largely ungauged and underrepresented within the model training (Ielpi and Lapôtre, 2022).

Model data for annual mean water discharge, Q [m^2/s], bedload sediment flux, $Q_{s,Bed}$[kg/s], and the suspended sediment flux that interacts with the bed, $Q_{s,SusBed}$ [kg/s], are available as netCDF files with 6-min spatial resolution (Cohen et al., 2013, 2022). We collected measurements of Q, $Q_{s,SusBed}$ and $Q_{s,Bed}$ for the closest downstream model cell for each study reach. Bar deposition is most closely related to total bed-material flux, that is the sediment flux interacting with the bed ($Q_{s,SusBed} + Q_{s,Bed}$) (Church, 2006). We focused on this quantity and report the total bed-material flux as Q_s throughout the manuscript. The WBMsed model produces estimates of sediment fluxes in kg/s, and we converted this to a volumetric sediment flux (m^3/yr) by assuming a bulk density of 1600 kg/m^3—a value previously used by Nienhuis and van de Wal (2021). We expect the uncertainty in the estimate of bulk sediment density to have minimal effect on our results because the bed-material sediment flux varies over several orders of magnitude across our dataset.

We computed the normalized sediment supply, Q_s^* (Eq. (5b)), using the modeled bed-material flux. We used estimated channel widths (Section 3.2), and measured meander wavelengths as two-times the distance between adjacent inflection points averaged across all bends included in the study reach. We recorded these values from the latest centerline in the image pair used for calculation of migration distances. We also examined the dimensionless sediment concentration, $Q_{s,c}$, as an alternative to Q_s^* following:

$$Q_{s,c} = \frac{Q_s}{\overline{Q}} \tag{6}$$

where $\overline{Q}$ is the long-term average water discharge from 1980 to 2020 computed from the WBMsed model. The long-term average water discharge scales with the bankfull channel volume (Leopold and Maddock, 1953) and provides an alternative companion to the expected volume normalization.

Measurements of bed-material sediment flux are empirically correlated to estimates of unit stream power, a metric quantifying the energy available per cross-sectional area to move sediment (Eaton and Church, 2011). Further, the relative efficiency of bedload transport per unit power is stratified by ephemeral and perennial hydrographs, which often correspond to differences in bank vegetation (Reid and Laronne, 1995). We examined relationships between normalized sediment supply and unit stream power within the WBMsed data. We calculated unit stream power as:

$$\omega = \frac{\rho g \overline{Q} S}{B} \tag{7}$$

where S is the channel bed slope, ρ is the fluid density in kg/m^3, and g is the acceleration due to gravity. We obtained estimates of S from the Global River Slope (GloRS) geospatial dataset (Cohen et al., 2018) from the same location as the WBMsed model cell. Finally, we used log-log regressions, a locally weighted regression, and two sample t-tests to examine relationships between the measured values of M_r, B, M_r^*, Q_s^*, $Q_{s,c}$, and ω (Supplementary Text S2).

3.4. Case studies from North American dammed rivers

Rivers with major downstream gradients in sediment supply provide an opportunity to isolate the role of sediment supply while controlling for other allogenic and autogenic influences on lateral migration rates. We paired our analysis with case studies of three well-documented North American rivers with dam impoundments (the Red River, Iowa River, and the Flint River; Fig. 1) to examine the impact of extreme downstream gradients in sediment supply on lateral migration rates.

We analyzed reaches of the Red River (Fig. 1(a)) upstream and downstream of Lake Texoma, an impoundment created by the Denison Dam (completed in 1943). We used a 494 km reach upstream of the lake from junction of the North Fork of the Red River with the Red River (34.3075, −99.2037) to Thackerville, OK (33.7221, −97.1452). While at low flows, upper portions of the Red River can appear bifurcated, single-thread processes are common at high flows. Scroll-bar formation and channel cutoffs are common throughout the studied reach upstream of Lake Texoma. There are portions of the upstream reach where the channel belt is confined to a ~1 km wide valley. We used a 551 km reach downstream of the lake from the area near Yarnaby, OK (33.7673, −96.2631) to the area near Lewisville, AR (33.3705, −93.7000). There are several major tributaries within the downstream reach: the Muddy Boggy Creek, the Kiamichi River, and the Little River. Two of these tributaries, the Kiamichi and the Little rivers, have major impoundments upstream of their junction with the Red River.

We analyzed reaches of the Iowa River upstream and downstream of Carolville Lake, formed behind the Carolville Dam (completed 1958) (Fig. 1(a)). We used a 62.5 km reach upstream of the lake from the area of Belle Plaine, IA (41.8611, −92.2830) to Amana, IA (41.7771, −91.8663). Downstream of Amana, IA, the floodplain is consistently inundated and the river forms a delta as the it flows into Carolville Lake. We used a 42.8 km reach downstream of the lake from Iowa City (41.6355, −91.5344) to the junction of the English River (41.4885, −91.5023). The extent of our downstream reach stops short of the English River junction to minimize the effects of any sediment supplied from the major tributary.

We also analyzed reaches of the Flint River upstream and downstream of Lake Blackshear, an impoundment formed behind the Crisp County Power Dam (completed 1930). We used a 72.4 km reach upstream of the lake from south of Georgia State Route 96 (32.5200, −84.0090) to North of Lake Blackshear (32.1051, −83.9995). Downstream of the dam, we used a 38.5 km reach from Warwick, GA (31.8384, −83.9578), to upstream of Lake Chehaw (31.6194, −84.0543), another impoundment.

For the upstream and downstream reaches of the Red River, Iowa River, and Flint River, we estimated channel widths, meander wave-

lengths, and migration rates between 1990 and 2020. We used the WBMsed model to estimate changes in bed-material flux across the impoundments. We sampled each 6-minute model cell that intersects with the study reaches and averaged bed-material flux estimates from 1980 to 2020. We used the median channel width and meander wavelength for a given reach to calculate Q_s^* (Eq. (5b)). To confirm that a difference in sediment supply is expected in natural data from upstream to downstream of the impoundment, we compared WBMsed results to published trends in sediment flux across the three impoundments. For the Red River, we used a U.S. Army Corps of Engineers report containing upstream and downstream suspended sediment concentration (Copeland, 2002). For the Iowa River, we used a published technical report on the sediment trapping efficiency (the percentage of sediment expected to be retained by the impoundment) of the Coralville Reservoir (Espinosa-Villegas and Schnoor, 2009). On the Flint River, the USGS has records of suspended sediment concentrations between January 1962 and September 1962 for two locations, upstream of the impoundment near Carsonville, GA (site number: 02347500), and downstream of the impoundment at Albany, GA (site number: 02352500). We used two-sample *t*-tests to test the hypotheses for differences in bend-scale measurements in upstream and downstream portions of the dammed rivers. We tested the null hypothesis that the mean M_r^* is equivalent upstream and downstream of the sediment-supply change.

4. Results

4.1. Comparing lateral river migration rates of meandering rivers across environmental settings

Measured M_r values from our database of 139 meandering rivers (Fig. 1(a)) range from 0.21 m/yr to 53.5 m/yr. These estimates represent temporal averages over 4 to 30 years. The normalized migration rates span $M_r^* \in [0.0037,\ 0.31]\ \mathrm{yr}^{-1}$. Study reaches have $S \in [1.6 \times 10^{-5},\ 5.8 \times 10^{-3}]$, long-term average water discharge and total bed-material flux of $\overline{Q} \in [0.1,\ 27341]\ \mathrm{m}^3/\mathrm{s}$ and $Q_s \in [0.07,\ 1087]$ kg/s, respectively. The estimated normalized sediment supply covered seven orders of magnitude, $Q_s^* \in [2 \times 10^{-5},\ 3 \times 10^{2}]\ \mathrm{yr}^{-1}$, and the dimensionless sediment concentration ranges from $Q_{s,c}^* \in [3 \times 10^{-6},\ 1.5 \times 10^{-2}]$.

Migration rates increase with increasing channel width across all reach-averaged data (Fig. 4(a)), consistent with previous work (Constantine et al., 2014; Hickin and Nanson, 1984; Ielpi and Lapôtre, 2020; Langhorst and Pavelsky, 2023). The dependence of migration rate on channel width appears stratified with bank vegetation (Fig. 4(a)), consistent with previous compilations specifically focusing on bank vegetation (Ielpi and Lapôtre, 2020, 2022). The reach-scale migration rates of rivers with unvegetated ($M_r = 0.20 \pm 0.1\ B^{0.71\ \pm\ 0.43}$; $R^2 = 0.524$) and vegetated banks ($M_r = 0.057 \pm 0.04\ B^{0.75\ \pm\ 0.16}$; $R^2 = 0.414$) show a similar dependence on channel width, where the scaling exponents of this relation are statistically similar ($P = 0.13$) but the pre-factor coefficients are statistically distinct ($P < 10^{-3}$). These results support the notion that at reach scales, bank vegetation regulates lateral migration

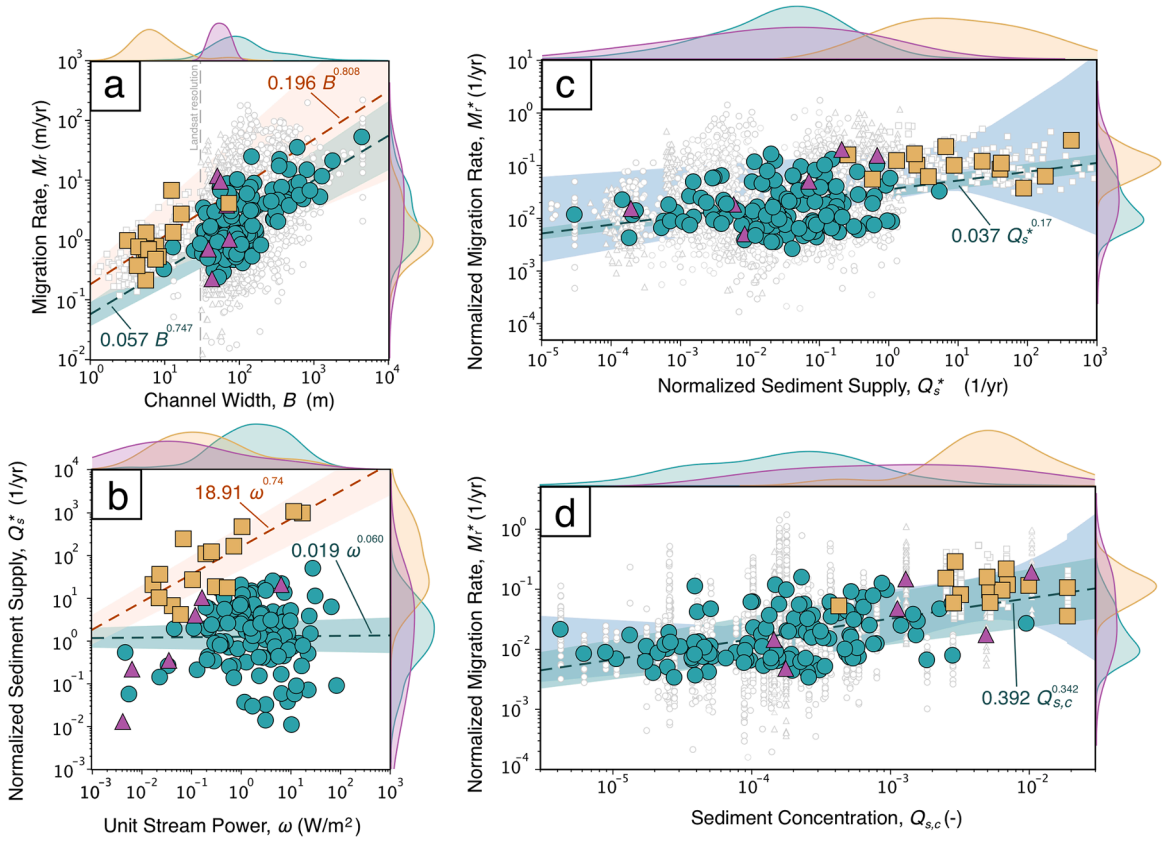

Fig. 4. Data from the worldwide lateral migration rate compilation. (a) Relationships between channel width and lateral migration rate for rivers with vegetated (teal), unvegetated (orange), and sparsely vegetated (purple) banks. Large symbols are reach-averaged data points, and light white symbols are bend-averaged data. Dotted lines and shaded regions indicate the mean and 95 % confidence intervals of the log-log regressions for rivers with vegetated and unvegetated banks, respectively. Empirical probability distribution functions are shown for each variable outside the data box grouped for floodplain vegetation type. The Landsat data resolution highlights the bias in river size within the data compilation. (b) The difference in normalized sediment supply for the same unit stream power for rivers in vegetated and unvegetated basins. The functional dependence of normalized migration rate on (c) normalized sediment supply, and (d) dimensionless sediment concentration (both quantities computed using modeled bed-material flux).

rates; however, the differences between migration rates of rivers with unvegetated and vegetated banks is smaller than the previously reported value of a factor of 10.7 (Ielpi and Lapôtre, 2020). Instead, the trend in our data indicate that river reaches of similar width migrate four times slower in vegetated basins when compared to their unvegetated counterparts.

Based on modeled WBMsed data combined with measured channel widths, rivers with unvegetated floodplains have an order-of-magnitude higher normalized sediment supply for the same unit stream power than rivers with vegetated floodplains (Fig. 4(b)). We find a positive relationship between Q_s^* and ω in rivers with unvegetated floodplains ($Q_s^* = 18.91 \pm 12.81\ \omega^{0.74\ \pm\ 0.48}$; $P = 0.005$; $R^2 = 0.49$), but no correlation between the two parameters in rivers with vegetated floodplains ($Q_s^* = 0.019 \pm 0.008\ \omega^{0.06\ \pm\ 0.23}$; $R^{2\ =}\ 0.002$). One explanation for the lack of correlation is that there are relatively few samples with low unit stream power and that the variability in the dataset overwhelms the strength of the relationship. The significant difference in pre-factor coefficients between the two regressions ($P < 10^{-3}$) indicates that within the WBMsed model, rivers in unvegetated catchments carry more sediment relative to their discharge and slope than their vegetated counterparts.

Our data compilation reveals a positive relation between the normalized lateral migration rate and normalized sediment supply over two orders of magnitude variation in M_r^*, and over seven orders of magnitude variation in Q_s^* (Fig. 4(c); $M_r^* = 0.037 \pm 0.01\ Q_s^{*0.17\ \pm\ 0.057}$; $R^{2\ =}\ 0.194$; $P < 10^{-3}$). The results indicate that M_r^* increases with normalized sediment supply from river-to-river at a global scale. A locally weighted regression (Loess) between M_r^* and Q_s^* demonstrates that there is no scaling break between these two variables across rivers with vegetated and unvegetated banks (Fig. 4(c)). Critically, the fastest migrating rivers within the dataset not only have unvegetated floodplains, but they also appear to be transporting the largest volumes of sediment relative to the size of their point bars. However, there is significant variability present in the relation between M_r^* and Q_s^*—only 20 % of the total variance in M_r^* is explained by Q_s^*. Finally, we find a positive correlation between the normalized lateral migration rate and the dimensionless sediment concentration, $Q_{s,c}$ (Fig. 4(d); $M_r^* = 0.392 \pm 0.3\ {Q_{s,c}}^{0.342\ \pm\ 0.087}$; $R^{2\ =}\ 0.301$; $P < 10^{-3}$). There is no break in scaling between the two variables across rivers with different bank vegetation.

4.2. Differences in lateral migration rates across three North American dammed rivers

We also find that the lateral migration rates respond to sediment supply changes across dams in the three North American rivers (Fig. 5). We find that the decrease in bed-material sediment flux caused by the dams along the Red, Flint, and Iowa rivers results in a decrease in lateral migration rate. We compare reaches upstream and downstream of Lake Texoma on the Red River (Fig. 5(a)). Upstream of the impoundment, $B \in [50,\ 450]$ m and lateral migration rates range from $M_r \in [0.2,\ 102]$ m/yr. This corresponds to normalized migration rates of $M_r^* \in [0.001,\ 0.738]\ \mathrm{yr}^{-1}$. Downstream of the impoundment, $B \in [84,\ 551]$ m, lateral migration rates range from $M_r \in [0.24,\ 47]$ m/yr, and normalized migration rates are $M_r^* \in [0.0008,\ 0.211]\ \mathrm{yr}^{-1}$. The decrease in median M_r^* from 0.037 yr^{-1} upstream to 0.013 yr^{-1} downstream is statistically significant (Fig. 5(b); $P < 10^{-3}$). Modeled bed-material flux increases from a median of 12.85 kg/s upstream to a median of 26.77 kg/s downstream of the dam. However, the median normalized sediment supply decreases (Fig. 5(c); $P = 0.03$) from 0.0067 yr^{-1} to 0.0029 yr^{-1} across the impoundment. An explanation is that the volume fluxes are averaged over the entire analyzed 551 km reach downstream of the dam, and that while absolute bed-material fluxes increase from multiple joining tributaries, increases in bed-material flux are less significant than increases in channel size, leading to a decrease in sediment

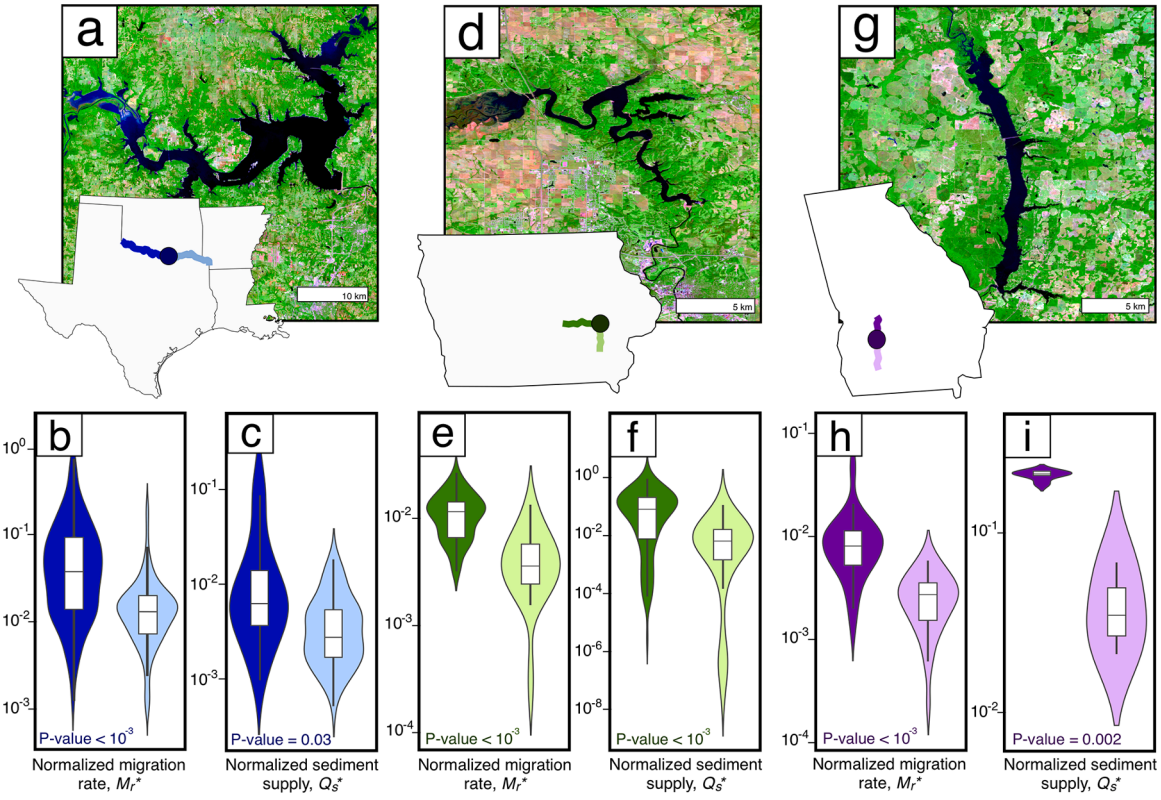

Fig. 5. Effect of river impoundments on lateral migration and sediment flux. Location of (a) Lake Texoma on the Red River (33.9045, −96.6211), (d) Coralville Lake on the Iowa River (41.7795, −91.5732), and (g) Lake Blackshear on the Flint River (31.9405, −83.9280). Violin and box plots showing the difference in M_r^* (b, e, h) and Q_s* (c, f, i) from upstream (left) to downstream (right) of the impoundment.

concentration. The WBMsed model results are consistent with the limited historical observations of suspended sediment from the Red River, which show sediment concentrations drop by 90 % from upstream to downstream of Lake Texoma, which is further exacerbated by the lack of unmanaged tributaries downstream of the dam (Copeland, 2002).

Upstream of Coralville Lake on the Iowa River (Fig. 5(d)), we find $B \in [33,\ 93]$ m and $M_r \in [0.15,\ 1.8]$ m/yr, which corresponds to normalized migration rates of $M_r^* \in [0.003,\ 0.026]$ yr^{-1}. Downstream of the impoundment, parameters range from $B \in [53,\ 82]$ m, $M_r \in [0.016,\ 0.87]$ m yr^{-1}, and $M_r^* \in [0.0002,\ 0.014]$ yr^{-1}. The downstream decrease in median M_r^* from 1.2×10^{-2} yr^{-1} to 3.7×10^{-3} yr^{-1} is statistically significant (Fig. 5(e); $P < 10^{-3}$). Modeled bed-material sediment flux also decreases across the impoundment from a median of 12.15 kg/s upstream to 2.52 kg/s downstream, and corresponds to a statistically significant ($P < 10^{-3}$) decrease in Q_s^* from 8.4 $\times 10^{-2}$ yr^{-1} to 6.9×10^{-3} yr^{-1} (Fig. 5(f)). Decreases in modeled bed-material fluxes are consistent with expectations; a previous study measures a decrease in average suspended sediment concentration (measured between 1980 and 2005) from 137.7 mg/l to 30.6 mg/l across the impoundment, with an average trapping efficiency of 74.7 % (Espinosa-Villegas and Schnoor, 2009). Differences in M_r^* and modeled Q_s^* are short lived downstream of Coralville Lake (41.4862, −91.5017). Both migration rates and modeled bed-material fluxes increase after the confluence of the English River, pointing to the influence of tributary sediment (Constantine et al., 2014).

There are similar changes in M_r^* and Q_s^* across Lake Blackshear on the Flint River (Fig. 5(g)). Upstream of the impoundment, we measure $B \in [33.7,\ 90.2]$ m, $M_r \in [0.06,\ 3.67]$ m/yr, and $M_r^* \in [0.001,\ 0.062]$ yr^{-1}. Downstream of the impoundment, we measure $B \in [51.8,\ 127.5]$ m, $M_r \in [0.016,\ 0.54]$ m/yr, and $M_r^* \in [0.0002,\ 0.005]$ yr^{-1}. The decrease in M_r^* from an upstream median of 0.008 yr^{-1} to 0.003 yr^{-1} downstream is statistically significant (Fig. 5(h); $P < 10^{-3}$). Modeled bed-material sediment flux also changes across the impoundment. Median modeled bed-material sediment flux decreases from 39.4 kg/s to 12.3 kg/s, which corresponds to a statistically significant decrease in Q_s^* ($P = 0.002$) from 0.21 yr^{-1} to 0.035 yr^{-1}. Median monthly sediment concentrations from USGS records also decrease from 0.03 kg/m^3 upstream of the impoundment to 0.017 kg/m^3 ($P = 0.039$).

5. Discussion

Our analysis reveals that the volumetric sediment flux relative to the size of the mobile landform—the point bar—is an important factor in channel migration (Fig. 4(c)). We find a positive relation between the normalized sediment supply, Q_s^*, and width-normalized lateral migration rates, M_r^*, for meandering rivers, which is consistent with downstream changes in lateral migration rate resulting from gradients in sediment supply imposed by major impoundments (Fig. 5). We find the same positive relationship when comparing sediment concentration, $Q_{s,c}^*$, and M_r^* (Fig. 4(d)). We suggest that the normalized sediment supply can be viewed a crude measure of the turnover rate for a bar-scale landform. Thus, our findings indicate that bar turnover rate is an important parameter for driving reach-scale variations in lateral migration, similar to the scaling between bed-material sediment flux and downstream dune migration rates (Bagnold, 1941).

Our findings demonstrate that sediment supply is potentially a primary driver of lateral migration rate, supporting previous findings of positive correlation between measured migration rates and total suspended sediment supply in the Amazon basin (Constantine et al., 2014; Ahmed et al., 2019). However, these results are in contrast with a recent remote sensing study that finds no correlation between sediment supply and bank migration in 16 river basins from the Amazon basin (Langhorst and Pavelsky, 2023). The migration rates in this study were calculated from the Riverbank Erosion and Accretion from Landsat (REAL) dataset, which measures lateral migration rates for all rivers with widths greater than 150 m. We posit that the differences in our results are likely a result of three study-design choices. First, limiting the analysis to rivers with width greater than 150 m is logical for REAL methodology, a programmatic method, but limits the river sizes represented in the dataset. For example, a similar size restriction would reduce our own database to just a quarter of its current size (Fig. 4(a)). Second, the REAL dataset aggregates migration rates over 10 km lengths to examine the effect of sediment supply. The 10 km reach aggregation is irrespective of river size, which means that for large rivers, the reach observation may only be representative of one or two bends. Third, the REAL dataset leverages the same source for sediment supply estimates, WBMsed, but treats sequential downstream estimates of sediment flux within a single river basin as independent measurements. Differences in modeled sediment supply will be most significant across river basins with differences in upstream drainage area, climate, and geology (Cohen et al., 2013). Together, comparing migration rates within a single river basin at 10 km increments implies that the expected range of estimated sediment supply is relatively low compared to the expected bend-scale variability in migration rate measurements, thus, limiting any potential signal of the influence of sediment supply on migration rates. To minimize potential noise-sources within our own dataset, we include rivers with a range of widths well below Landsat resolution (30 m), aggregate migration rates at length-scales that encompasses more than 15 bends for all rivers, and evaluate the sediment supply control across basins and climate zones, not just within them.

Our data compilation provides further insight into the relative role of sediment supply and floodplain vegetation in driving trends in meander migration rates and suggests that floodplain vegetation is not solely responsible for setting broad-scale trends in lateral migration rates. We find that rivers with unvegetated banks migrate four times faster than their vegetated counterparts for the same width (Fig. 4(a)). While this trend is consistent with previous work (Ielpi and Lapôtre, 2020), we also find that rivers with unvegetated banks within the dataset carry large volumes of sediment relative to their size. These WBMsed results (Fig. 4(b)) are consistent with field observation of natural rivers, which show that ephemeral rivers—typical of unvegetated, arid environments—carry significantly larger proportions of bedload flux when compared to perennial rivers for a given unit stream power (Laronne and Reid, 1993), and that rivers across arid regions typically carry more suspended sediment for the same water discharge (Chapman and Finnegan, 2024).

We pose an alternative hypothesis: the faster lateral migration rates observed in meandering rivers throughout unvegetated basins could be a result of the larger relative bed-material load carried by ephemeral rivers, such that the bar accretion rates are high. This hypothesis does not minimize the importance of vegetation in setting the pace of river mobility. Vegetation could have a first-order control on bank erodibility (Ielpi et al., 2022). However, meandering planform stability is driven by dynamic equilibrium in bank erosion and bar deposition (Mason and Mohrig, 2019). Recent experimental work demonstrates that multi-thread river planforms (e.g. braided) arise from a dynamic state of runaway thread widening (Chadwick et al., 2022), indicating that rivers in unvegetated environments that have rapid bank erosion rates in excess of bar deposition rates will follow a state of runaway widening, leading to multi-thread river planform instead of maintaining a stable meandering planform. This hypothesis is difficult to directly address with the dataset presented here and a key constraint is that the represented unvegetated and vegetated rivers have nonoverlapping widths. Our dataset only includes two vegetated rivers (Rivers Exe and Teme) with widths comparable to unvegetated rivers, and one unvegetated river (Sulengguole River) with a width comparable to vegetated rivers. The overlapping cases, however, have qualitatively similar normalized migration rates for the same width (Fig. 4(a)), supporting our hypothesis. The availability of commercial remote sensing products can provide decadal records of Earth surface change at <5 m resolution and could be a powerful resource to build a dataset of small (<30 m wide), vegetated

meandering river lateral migration rates, which could help directly address the relative importance of floodplain vegetation and sediment supply in setting the pace of meander migration.

Finally, our results can provide constraints on how rivers may respond or have responded to projected and past environmental changes. Specifically, the importance of sediment supply in determining reach-scale migration rates sets expectations for how rivers will respond to anthropogenically-forced changes in fluvial boundary conditions. Expected shifts in extreme precipitation (Papalexiou and Montanari, 2019) could increase both net and peak sediment supply, which can be magnified by feedbacks between extreme precipitation and increased channel cutoff events that enhance sediment supply (Zinger et al., 2011). Similarly, land-use changes such as watershed deforestation can increase sediment supply—a trend already observed in large rivers throughout the southern hemisphere (Dethier et al., 2022). If perturbations to the sediment cycle do not impact river planform stability, changes in river sediment flux could impact lateral migration rates in meandering rivers at regional scales. However, the nature of expected river changes in response to sediment supply shifts is likely to be complex. For example, river responses to sediment waves and deficits arising from the removal and construction of dams not only cause changes in river mobility, but also geometric changes from channel incision (Williams and Wolman, 1984) or more drastic planform changes (Słowik et al., 2018). Moreover, past extreme greenhouse climate events like the Paleocene-Eocene Thermal Maximum (PETM; ~56 Ma; see McInerney and Wing, 2011) are interpreted to correspond to an increase in net export of sediment to the world's ocean basins, and therefore increased terrestrial sediment supply (John et al., 2008). Our results indicate that such an increase in sediment supply could accelerate lateral migration rates, which is often used to explain large-scale poorly preserved fluvial sandstone deposits ubiquitous during the PETM interval (Barefoot et al., 2021; Foreman et al., 2012).

6. Conclusions

We used a data compilation and case study examples to highlight the role of sediment supply in controlling reach-to-reach variability in lateral migration rates of meandering rivers. We examined reach-averaged migration rates for 139 rivers worldwide, and showed that width-normalized migration rates increase monotonically with increase in both volume-normalized sediment supply (Fig. 4(c)) and sediment concentration (Fig. 4(d)). While rivers without floodplain vegetation migrate faster for a given width (Fig. 4(a)), the signal could be explained by high bed-material fluxes in arid catchments (Fig. 4(b)). We show three case examples of statistically significant decreases in normalized lateral migration rates across dam impoundments that correspond to significant shifts in sediment supply (Fig. 5). Together, this work supports the hypothesis that sediment flux is a primary environmental control on lateral migration rates in meandering rivers.

Data availability

The codes underlying this study are publicly available in an archived Zenodo repository at DOI: https://doi.org/10.5281/zenodo.8341862. The software used to generate binary channel water masks can be found at DOI: https://doi.org/10.5281/zenodo.7747389. All Landsat and centerline-vector data used to calculate migration rates as well as the full tabular data used in the analysis can be found in the Dryad repository: DOI https://doi.org/10.5061/dryad.jq2bvq8g3. WBMsed water discharge and sediment flux estimates were provided by Sagy Cohen.

CRediT authorship contribution statement

Evan Greenberg: Writing – review & editing, Writing – original draft, Visualization, Validation, Software, Resources, Project administration, Methodology, Investigation, Formal analysis, Data curation, Conceptualization. **Vamsi Ganti:** Writing – review & editing, Writing – original draft, Validation, Supervision, Resources, Project administration, Investigation, Funding acquisition, Formal analysis.

Declaration of competing interest

The authors declare that they have no known competing financial interests or personal relationships that could have appeared to influence the work reported in this paper.

Acknowledgments

We thank Sagy Cohen for sharing the water and sediment data, and Tom Dunne, Austin Chadwick, and Michael Lamb for insightful discussions. We also thank Eric Barefoot and Tim Goudge for constructive comments on a previous draft. This work was supported by the National Science Foundation grants EAR 1935669 and EAR 2310740 to Ganti.

Supplementary materials

Supplementary material associated with this article can be found, in the online version, at doi:10.1016/j.epsl.2024.118674.

References

Ahmed, J., Constantine, J.A., Dunne, T., 2019. The role of sediment supply in the adjustment of channel sinuosity across the Amazon Basin. Geology 47 (9), 807–810. https://doi.org/10.1130/G46319.1.

Allen, G.H., Pavelsky, T.M., 2018. Global extent of rivers and streams. Science 361 (6402), 585–588.

Bagnold, R.A., 1941. The Physics of Blown Sand and Desert Dune. Methuen.

Barefoot, E.A., Nittrouer, J.A., Foreman, B.Z., Hajek, E.A., Dickens, G.R., Baisden, T., Toms, L., 2021. Evidence for enhanced fluvial channel mobility and fine sediment export due to precipitation seasonality during the Paleocene-Eocene thermal maximum. Geology 50 (1), 116–120. https://doi.org/10.1130/G49149.1.

Best, J., 2019. Anthropogenic stresses on the world's big rivers. Nat. Geosci. 12 (1), 7–21.

Braudrick, C.A., Dietrich, W.E., Leverich, G.T., Sklar, L.S., 2009. Experimental evidence for the conditions necessary to sustain meandering in coarse-bedded rivers. Proc. Natl. Acad. Sci. 106 (40), 16936–16941.

Bufe, A., Turowski, J.M., Burbank, D.W., Paola, C., Wickert, A.D., Tofelde, S., 2019. Controls on the lateral channel-migration rate of braided channel systems in coarse non-cohesive sediment. Earth Surf. Process. Landf. 44 (14), 2823–2836.

Cardenas, B.T., Mohrig, D., Goudge, T.A., 2017. Fluvial stratigraphy of valley fills at Aeolis Dorsa, Mars: evidence for base-level fluctuations controlled by a downstream water body. GSA Bull. 130 (3–4), 484–498. https://doi.org/10.1130/B31567.1.

Chadwick, A.J., Steel, E., Passalacqua, P., Paola, C., 2022. Differential bank migration limits the lifespan and width of braided channel threads. Water Resour. Res. 58 (8) e2021WR031236.

Chadwick, A.J., Greenberg, E., Ganti, V., 2023. Remote sensing of riverbank migration using particle image velocimetry. J. Geophys. Res. 128 (7) https://doi.org/10.1029/2023JF007177 e2023JF007177.

Chapman, W.A.L., Finnegan, N.J., 2024. The signature of climate in fluvial suspended sediment records. J. Geophys. Res. 129 (1) https://doi.org/10.1029/2023JF007429 e2023JF007429.

Church, M., 2006. Bed material transport and the morphology of alluvial river channels. Annu. Rev. Earth Planet. Sci. 34, 325–354.

Cohen, S., Kettner, A.J., Syvitski, J.P., Fekete, B.M., 2013. WBMsed, a distributed global-scale riverine sediment flux model: model description and validation. Comput. Geosci. 53, 80–93.

Cohen, S., Kettner, A.J., Syvitski, J.P.M., 2014. Global suspended sediment and water discharge dynamics between 1960 and 2010: continental trends and intra-basin sensitivity. Glob. Planet. Change 115, 44–58. https://doi.org/10.1016/j.gloplacha.2014.01.011.

Cohen, S., Wan, T., Islam, M.T., Syvitski, J.P.M., 2018. Global river slope: a new geospatial dataset and global-scale analysis. J. Hydrol. 563, 1057–1067. https://doi.org/10.1016/j.jhydrol.2018.06.066.

Cohen, S., Syvitski, J., Ashley, T., Lammers, R., Fekete, B., Li, H., 2022. Spatial trends and drivers of bedload and suspended sediment fluxes in global rivers. Water Resour. Res. 58 (6) e2021WR031583.

Constantine, J.A., Dunne, T., Ahmed, J., Legleiter, C., Lazarus, E.D., 2014. Sediment supply as a driver of river meandering and floodplain evolution in the Amazon Basin. Nat. Geosci. 7 (12), 899–903.

Copeland, R.R., 2002. Red River Below Denison Dam, Texas, Oklahoma, Arkansas, and Louisiana. U.S. Army Corps of Engineers.

Dethier, E.N., Renshaw, C.E., Magilligan, F.J., 2022. Rapid changes to global river suspended sediment flux by humans. Science 376 (6600), 1447–1452. https://doi.org/10.1126/science.abn7980.

Dietrich, W.E., Smith, J.D., 1983. Influence of the point bar on flow through curved channels. Water Resour. Res. 19 (5), 1173–1192.
Donovan, M., Belmont, P., Sylvester, Z., 2021. Evaluating the relationship between meander-bend curvature, sediment supply, and migration rates. J. Geophys. Res. 126 (3) e2020JF006058.
Eaton, B.C., Church, M., 2011. A rational sediment transport scaling relation based on dimensionless stream power. Earth Surf. Process. Landf. 36 (7), 901–910. https://doi.org/10.1002/esp.2120.
Espinosa-Villegas, C.O., Schnoor, J.L., 2009. Comparison of long-term observed sediment trap efficiency with empirical equations for Coralville Reservoir, Iowa. J. Environ. Eng. 135 (7), 518–525. https://doi.org/10.1061/(ASCE)0733-9372(2009)135:7(518).
Foreman, B.Z., Heller, P.L., Clementz, M.T., 2012. Fluvial response to abrupt global warming at the Palaeocene/Eocene boundary. Nature 491 (7422), 92–95.
Furbish, D.J., 1988. River-bend curvature and migration: how are they related? Geology 16 (8), 752. https://doi.org/10.1130/0091-7613(1988)016<0752:RBCAMH>2.3.CO;2.
Gomez-Velez, J.D., Harvey, J.W., Cardenas, M.B., Kiel, B., 2015. Denitrification in the Mississippi River network controlled by flow through river bedforms. Nat. Geosci. 8 (12), 941–945. https://doi.org/10.1038/ngeo2567.
Gorelick, N., Hancher, M., Dixon, M., Ilyushchenko, S., Thau, D., Moore, R., 2017. Google earth engine: planetary-scale geospatial analysis for everyone. Remote Sens. Environ. 202, 18–27. https://doi.org/10.1016/j.rse.2017.06.031.
Greenberg, E., Ganti, V., Hajek, E., 2021. Quantifying bankfull flow width using preserved bar clinoforms from fluvial strata. Geology 49 (9), 1038–1043. https://doi.org/10.1130/G48729.1.
Hickin, E.J., Nanson, G.C., 1984. Lateral migration rates of river bends. J. Hydraul. Eng. 110 (11), 1557–1567.
Holzweber, B.I., Hartley, A.J., Weissmann, G.S., 2014. Scale invariance in fluvial barforms: implications for interpretation of fluvial systems in the rock record. Pet. Geosci. 20 (2), 211–224. https://doi.org/10.1144/petgeo2011-056.
Ielpi, A., Lapôtre, M.G., 2020. A tenfold slowdown in river meander migration driven by plant life. Nat. Geosci. 13 (1), 82–86.
Ielpi, A., Lapôtre, M.G., 2022. Linking sediment flux to river migration in arid landscapes through mass balance. J. Sediment. Res. 92 (8), 695–703.
Ielpi, A., Lapôtre, M.G., Gibling, M.R., Boyce, C.K., 2022. The impact of vegetation on meandering rivers. Nat. Rev. Earth Environ. 3 (3), 165–178.
Ikeda, S., Parker, G., Sawai, K., 1981. Bend theory of river meanders. Part 1. Linear development. J. Fluid Mech. 112, 363–377.
John, C.M., Bohaty, S.M., Zachos, J.C., Sluijs, A., Gibbs, S., Brinkhuis, H., Bralower, T.J., 2008. North American continental margin records of the Paleocene-Eocene thermal maximum: implications for global carbon and hydrological cycling: continental margin records of the PETM. Paleoceanography 23 (2). https://doi.org/10.1029/2007PA001465 n/a-n/a.
Jones, J.W., 2019. Improved automated detection of subpixel-scale inundation—Revised dynamic surface water extent (DSWE) partial surface water tests. Remote Sens. 11 (4), 374.
Lammers, R.W., Bledsoe, B.P., 2018. Parsimonious sediment transport equations based on Bagnold's stream power approach. Earth Surf. Process. Landf. 43 (1), 242–258. https://doi.org/10.1002/esp.4237.
Langhorst, T., Pavelsky, T., 2023. Global observations of riverbank erosion and accretion from landsat imagery. J. Geophys. Res. 128 (2) https://doi.org/10.1029/2022JF006774 e2022JF006774.
Laronne, J.B., Reid, L., 1993. Very high rates of bedload sediment transport by ephemeral desert rivers. Nature 366 (6451), 148–150. https://doi.org/10.1038/366148a0.
Legleiter, C.J., Roberts, D.A., Lawrence, R.L., 2009. Spectrally based remote sensing of river bathymetry. Earth Surf. Process. Landf. 34 (8), 1039–1059. https://doi.org/10.1002/esp.1787.
Lehner, B., Verdin, K., Jarvis, A., 2008. New global hydrography derived from spaceborne elevation data. Eos, Trans. Am. Geophys. Union 89 (10), 93–94. https://doi.org/10.1029/2008EO100001.
Leopold, L.B., Maddock, T., 1953. The Hydraulic Geometry of Stream Channels and Some Physiographic Implications, 252. US Government Printing Office.
Mason, J., Mohrig, D., 2019. Differential bank migration and the maintenance of channel width in meandering river bends. Geology 47 (12), 1136–1140. https://doi.org/10.1130/G46651.1.
McInerney, F.A., Wing, S.L., 2011. The paleocene-eocene thermal maximum: a perturbation of carbon cycle, climate, and biosphere with implications for the future. Annu. Rev. Earth Planet. Sci. 39, 489–516.
Micheli, E.R., Kirchner, J.W., 2002. Effects of wet meadow riparian vegetation on streambank erosion. 2. Measurements of vegetated bank strength and consequences for failure mechanics. Earth Surf. Process. Landf. 27 (7), 687–697. https://doi.org/10.1002/esp.340.
Micheli, E.R., Kirchner, J.W., Larsen, E.W., 2004. Quantifying the effect of riparian forest versus agricultural vegetation on river meander migration rates, central Sacramento River, California, USA. River Res. Appl. 20 (5), 537–548. https://doi.org/10.1002/rra.756.
Mohrig, D., Heller, P.L., Paola, C., Lyons, W.J., 2000. Interpreting avulsion process from ancient alluvial sequences: Guadalope–Matarranya system (northern Spain) and wasatch formation (western Colorado). Geol. Soc. Am. Bull. 112 (12), 1787–1803.
Neill, C.R., 1971. River bed transport related to meander migration rates. J. Waterw., Harb.Coast. Eng. Div. 97 (4), 783–786.
Nienhuis, J.H., van de Wal, R.S.W., 2021. Projections of global delta land loss from sea-level rise in the 21st century. Geophys. Res. Lett. 48 (14) https://doi.org/10.1029/2021GL093368 e2021GL093368.
Ollero, A., 2010. Channel changes and floodplain management in the meandering middle Ebro River, Spain. Geomorphology 117 (3–4), 247–260.
Papalexiou, S.M., Montanari, A., 2019. Global and regional increase of precipitation extremes under global warming. Water Resour. Res. 55 (6), 4901–4914. https://doi.org/10.1029/2018WR024067.
Peel, M.C., Finlayson, B.L., McMahon, T.A., 2007. Updated world map of the Köppen–Geiger climate classification. Hydrol. Earth Syst. Sci. 11 (5), 1633–1644.
Reid, I., Laronne, J.B., 1995. Bed load sediment transport in an ephemeral stream and a comparison with seasonal and perennial counterparts. Water Resour. Res. 31 (3), 773–781. https://doi.org/10.1029/94WR02233.
Repasch, M., Scheingross, J.S., Hovius, N., Lupker, M., Wittmann, H., Haghipour, N., et al., 2021. Fluvial organic carbon cycling regulated by sediment transit time and mineral protection. Nat. Geosci. 14 (11), 842–848. https://doi.org/10.1038/s41561-021-00845-7.
Rowland, J.C., Shelef, E., Pope, P.A., Muss, J., Gangodagamage, C., Brumby, S.P., Wilson, C.J., 2016. A morphology independent methodology for quantifying planview river change and characteristics from remotely sensed imagery. Remote Sens. Environ. 184, 212–228.
Schwenk, J., Khandelwal, A., Fratkin, M., Kumar, V., Foufoula-Georgiou, E., 2017. High spatiotemporal resolution of river planform dynamics from Landsat: the RivMAP toolbox and results from the Ucayali River. Earth Space Sci. 4 (2), 46–75. https://doi.org/10.1002/2016EA000196.
Sekine, M., Parker, G., 1992. Bed-load transport on transverse slope. I. J. Hydraul. Eng. 118 (4), 513–535.
Słowik, M., Dezső, J., Marciniak, A., Tóth, G., Kovács, J., 2018. Evolution of river planforms downstream of dams: effect of dam construction or earlier human-induced changes? Earth Surf. Process. Landf. 43 (10), 2045–2063. https://doi.org/10.1002/esp.4371.
Struiksma, N., Olesen, K.W., Flokstra, C., De Vriend, H.J., 1985. Bed deformation in curved alluvial channels. J. Hydraul. Res. 23 (1), 57–79.
Sylvester, Z., Durkin, P., Covault, J.A., 2019. High curvatures drive river meandering. Geology 47 (3), 263–266.
Tal, M., Paola, C., 2007. Dynamic single-thread channels maintained by the interaction of flow and vegetation. Geology 35 (4), 347–350.
Torres, M.A., Limaye, A.B., Ganti, V., Lamb, M.P., West, A.J., Fischer, W.W., 2017. Model predictions of long-lived storage of organic carbon in river deposits. Earth Surf. Dyn. 5 (4), 711–730.
Turowski, J.M., Rickenmann, D., Dadson, S.J., 2010. The partitioning of the total sediment load of a river into suspended load and bedload: a review of empirical data. Sedimentology 57 (4), 1126–1146. https://doi.org/10.1111/j.1365-3091.2009.01140.x.
Wickert, A.D., Martin, J.M., Tal, M., Kim, W., Sheets, B., Paola, C., 2013. River channel lateral mobility: metrics, time scales, and controls. J. Geophys. Res. 118 (2), 396–412.
Williams, G.P., Wolman, M.G., 1984. Downstream Effects of Dams on Alluvial Rivers, 1286. US Government Printing Office.
Wisser, D., Fekete, B.M., Vörösmarty, C.J., Schumann, A.H., 2010. Reconstructing 20th century global hydrography: a contribution to the global terrestrial network-hydrology (GTN-H). Hydrol. Earth Syst. Sci. 14 (1), 1–24. https://doi.org/10.5194/hess-14-1-2010.
Yang, X., Pavelsky, T.M., Allen, G.H., Donchyts, G., 2019. RivWidthCloud: an automated Google Earth Engine algorithm for river width extraction from remotely sensed imagery. IEEE Geosci. Remote Sens. Lett. 17 (2), 217–221.
Zhu, T., Lund, J.R., Jenkins, M.W., Marques, G.F., Ritzema, R.S., 2007. Climate change, urbanization, and optimal long-term floodplain protection. Water Resour. Res. 43 (6) https://doi.org/10.1029/2004WR003516.
Zinger, J.A., Rhoads, B.L., Best, J.L., 2011. Extreme sediment pulses generated by bend cutoffs along a large meandering river. Nat. Geosci. 4 (10), 675–678.